

A Contrastive Learning Foundation Model Based on Perfectly Aligned Sample Pairs for Remote Sensing Images

Hengtong Shen^a, Haiyan Gu^a, Haitao Li^a, Yi Yang^a, Agen Qiu^a

^aChinese Academy of Surveying and Mapping, Key Laboratory of Surveying and Mapping Science and Geospatial Information Technology, MNR, Beijing, China

ABSTRACT

Self-Supervised Learning (SSL) enables us to pre-train foundation models without costly labeled data. Among SSL methods, Contrastive Learning (CL) methods are better at obtaining accurate semantic representations in noise interference. However, due to the significant domain gap, while CL methods have achieved great success in many computer vision tasks, they still require specific adaptation for Remote Sensing (RS) images. To this end, we present a novel self-supervised method called **PerA**, which produces all-purpose RS features through semantically **P**erfectly **A**ligned sample pairs. Specifically, PerA obtains features from sampled views by applying spatially disjoint masks to augmented images rather than random cropping. Our framework provides high-quality features by ensuring consistency between teacher and student and predicting learnable mask tokens. Compared to previous contrastive methods, our method demonstrates higher memory efficiency and can be trained with larger batches due to its sparse inputs. Additionally, the proposed method demonstrates remarkable adaptability to uncurated RS data and reduce the impact of the potential semantic inconsistency. We also collect an unlabeled pre-training dataset, which contains about 5 million RS images. We conducted experiments on multiple downstream task datasets and achieved performance comparable to previous state-of-the-art methods with a limited model scale, demonstrating the effectiveness of our approach. We hope this work will contribute to practical remote sensing interpretation works.

KEYWORDS: Remote Sensing, Contrastive Learning, Foundation model, Self-Supervised, Deep Learning

1. Introduction

In recent years, deep learning approaches have increasingly become the primary means for ground surface interpretation tasks such as natural resource surveys (Pei T, Xu J, Liu Y, et al. 2021; Chen Y, Fan R, Yang X, et al.

2018), crop monitoring (Nguyen T T, Hoang T D, Pham M T, et al. 2020), and ecological environment protection (Yuan Q, Shen H, Li T, et al. 2020). However, relying on manually labeled Remote Sensing (RS) data, it is difficult to match the dataset scale to increasingly large models. To address this issue, many Self-Supervised Learning (SSL) methods have been employed to leverage the vast amount of unlabeled RS data available (Reed C J, Gupta R, Li S, et al. 2023; Stojnic V, Risojevic V. 2021). Using well-designed pretext tasks, SSL methods produce pseudo-labels to learn general and intelligible representations (Geiping J, Garrido Q, Fernandez P, et al. 2023). Among the two main categories of SSL, generative and contrastive, Contrastive Learning (CL) is more competitive in image linear classification (Chen X, Xie S, He K. 2021). By distinguishing between similar and dissimilar data points, CL methods learn global-level semantics from large amounts of data and significantly enhance the model's representational capabilities. Although numerous works have explored applying CL methods to RS images, these methods are typically designed for natural images, which differ significantly from RS images. Specifically, these differences can be summarized as follows:

- (1) RS images are captured by various sensors, resulting in significant domain distance between them and natural images.
- (2) RS images are taken from bird's eye view, which causes a large gap in spatial resolution compared to natural images. Many different categories of objects in RS images are usually small and scattered.
- (3) RS image samples are usually uncurated, as they are obtained by cropping large-size RS imagery. Unlike most natural image datasets, these wild samples are neither object-centered nor category-balanced.

These properties of RS images make it difficult to transfer good features from models pre-trained on natural image datasets like ImageNet (Wang D, Zhang J, Du B, et al.

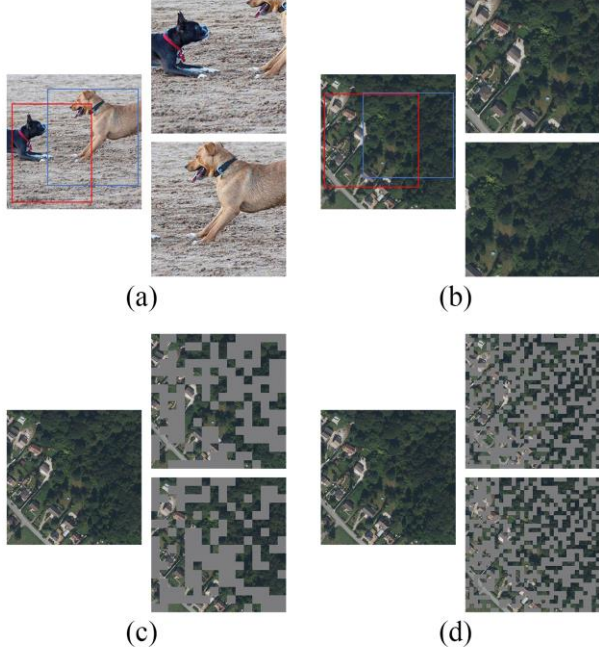


Figure 1. Random cropped views on ImageNet and Random masked on uncured RS images. (a) Objects do not correspond to in random cropped views on ImageNet; (b) Objects do not correspond to in random cropped views on RS images; (c) Objects correspond to in 32×32 patch random masked views on RS images; (d) Objects correspond to in 16×16 patch random masked views on RS images.

2022). Besides, most CL methods are based on instance discrimination and similar pretext tasks, which consider augmented images as different views (crops) and encourage similarity between them. As shown in Figure 1(a) and (b), due to random cropping, this can lead to potential semantic inconsistencies, especially in RS images (Muhtar D, Zhang X, Xiao P. 2022; Jean N, Wang S, Samar A, et al. 2019). After randomly cropping, two views from one RS image tend to have irrelevant categories. These limitations call for more efficient and RS-adapted methods to develop a better feature extractor with unlabeled RS data.

To achieve more precise semantics, many studies have started examining the effective underlying mechanisms of contrastive learning (CL) approaches and understanding how they extract features from unlabeled data (Wang T, Isola P. 2020; Ji W, Deng Z, Nakada R, et al. 2023). A reasonable interpretation is that, with much stronger data augmentations, CL methods attempt to find correlations between sparse signals and separate them from spurious dense noise. Since different coordinate of dense noise are independent to each other, we can decorrelate the dense noise by randomly applying two

completely opposite masks to images that learn better representations as much as possible (Wen Z, Li Y. 2021). Moreover, with random masks, these positive pairs come from the same original image, making them semantically aligned but inconsistent in appearance. As shown in Figure 1 (c) and (d), randomly masked samples rarely result in semantic inconsistencies, even in uncured RS images containing tiny objects. As the size of the mask units (patch size) decreases, the probability of generating semantically inconsistent sample pairs decreases as well, since objects in RS images are less likely to be masked completely. Once the patch size is reduced to be smaller than the smallest object in the image, the semantic information between sample pairs will be identical.

Numerous works have found that CL methods learn better global representations by capturing relations between positive sample pairs, resulting in better performance in global classification tasks (Muhtar D, Zhang X, Xiao P, et al. 2023). However, they sometimes lack ability in dense prediction tasks like object detection (Li Y, Xie S, Chen X, et al. 2021). In contrast, Masked Image Modeling (MIM) methods, which learn representations by reconstructing the missing information or features from the masked image, are usually less suited for linear classification, but exhibit robust dense prediction capabilities (Zhou Q, Yu C, Luo H, et al. 2022; Huang Z, Jin X, Lu C, et al. 2023). From a certain point of view, CL and MIM methods complement each other. Additionally, the reconstructing ability of MIM benefits sparse input, which is likely to be masked partly. These motivate us to propose a new RS pre-training framework that accepts sparse image inputs and combines CL and MIM methods. In this study, we present PerA, a simple but effective remote sensing Contrastive Learning method that processes sparse sample pairs which are Perfectly Aligned in semantics. PerA fully leverages the advantages of CL, MIM, and sparse semantic information, so that it can adapt to most common uncured RGB remote sensing images. To ensure that the model has sufficient training data to learn a general and effective representation, we designed a data processing pipeline to obtain unlabeled RS images for pre-training and collected a RS pre-training dataset, which contains about 5 million unlabeled RS images. RS images in the dataset, were captured from satellite maps, ranging in spatial resolution from 2 to 10 m. Thanks to the global land cover products of high accuracy, these images cover six continents and are balanced in categories. Based on the pre-training dataset and PerA, we trained a RS foundation model with unlabeled images, which can obtain features with accurate semantic information and can be widely used in a variety of downstream tasks. We evaluate our model on AID dataset (Xia G S, Hu J, Hu F, et al. 2017), ISPRS Potsdam dataset (Sherrah J. 2016) and LEVIR-CD

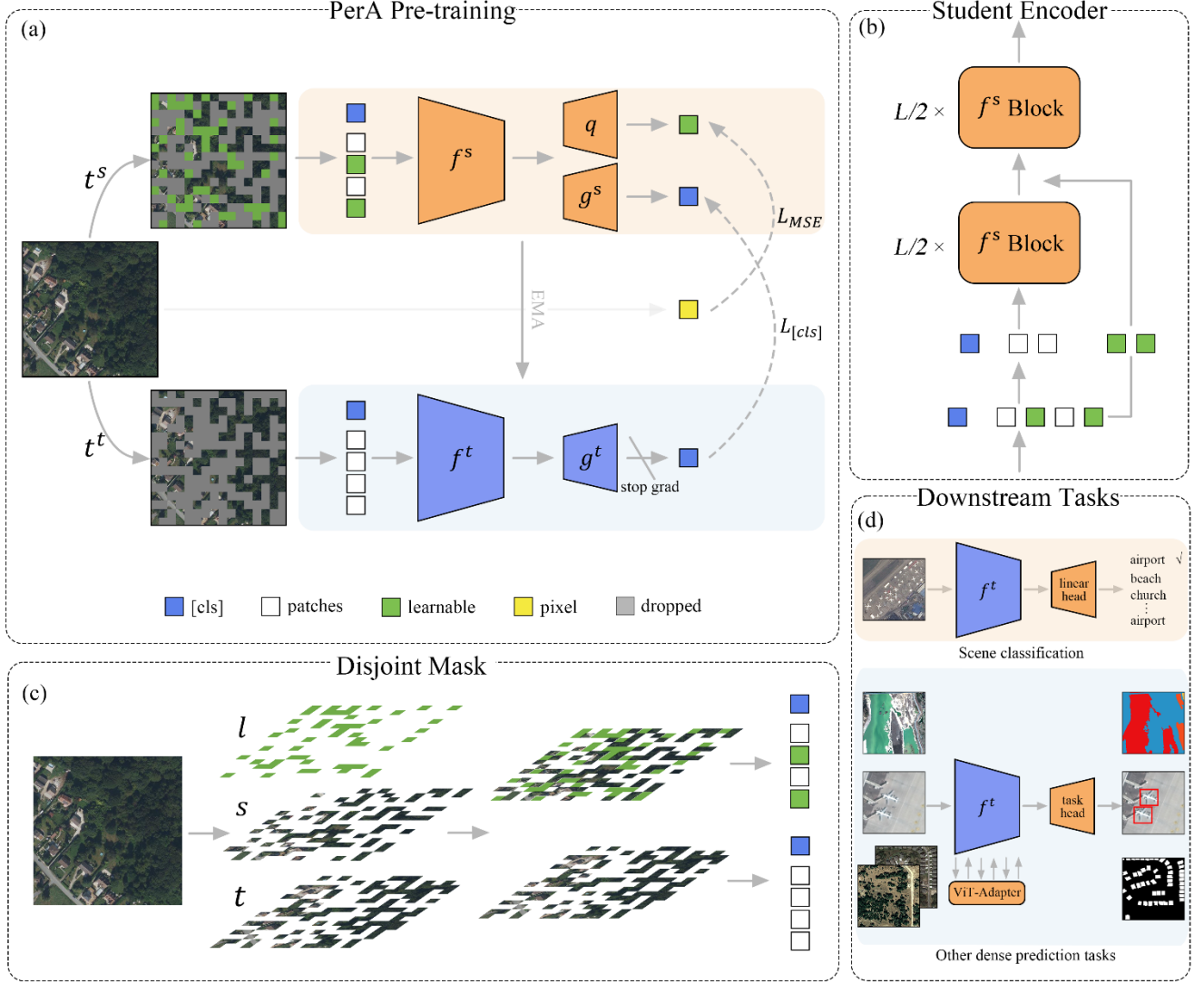


Figure 2. Illustration of PerA (a) pre-training, (b) student encoder structure, and (c) disjoint mask, (d) fine-tuning on downstream interpretation tasks.

(Chen H, Shi Z. 2020) dataset, etc., achieving competitive results in every downstream task.

In conclusion, our main contributions can be summarized as follows:

- (1) We developed an automatic pipeline for capturing unlabeled pre-training data. By random sampling, we obtained around 5 million unlabeled RS images globally and compiled them into the dataset RSRSD-5m. To the best of our knowledge, this is one of the largest publicly available unlabeled RS datasets.
- (2) We designed a novel method called PerA, which is tailored to the characteristics of remote sensing images. It demonstrates that sparse sample pairs with perfectly aligned semantics improve transfer performance and representation capabilities.

- (3) Extensive experiments across various downstream tasks, including image classification, semantic segmentation, and change detection, show that our pre-training framework achieves comparable to or even surpassing previous state-of-the-art results, which verify the superiority of our method.

2. Related work

In this section, we mainly introduce relevant works of Contrastive Learning methods in RS and Computer Vision (CV). Finally, we discuss currently available methods used to resolve semantic inconsistencies in CL.

2.1. Contrastive Learning methods in CV

The idea of a Contrastive Learning (CL), which encouraging similarity between semantic features, was

first introduced in (Bromley J, Guyon I, LeCun Y, et al. 1993). However, it was not until recent significant works that CL achieved groundbreaking progress in the field of CV. By discriminating among individual instances, CL methods can learn more general representations (Wu Z, Xiong Y, Yu S X, et al. 2018). Nevertheless, early CL methods like CMC (Tian Y, Krishnan D, Isola P. 2020) and SimCLR (Chen T, Kornblith S, Norouzi M, et al. 2020) struggled with storing vast high-dimensional signals of negative samples. These methods either simply employ huge batch sizes, which consume a tremendous amount of computational resources, or rely on a memory bank, which can cause representation irrelevance. These issues were not solved until MoCo (He K, Fan H, Wu Y, et al. 2020) was proposed. MoCo utilizes a queue and a moving-averaged encoder to build a large and consistent dictionary of sample pairs. The memory-efficient queue provides sufficient negative samples while the slowly updated moving-averaged encoder ensures that representations come from similar extractors. MoCo successfully suggested that CL methods can still reach competitive results with unlabeled data only.

To store representations of negative samples, these methods designed different frameworks to get a large dictionary with extensive semantic information. However, BYOL (Grill J B, Strub F, Altché F, et al. 2020), an approach that simply adds a linear predictor head to the classic CL structure, demonstrates that CL methods can learn meaningful information only with positive sample pairs. As long as the model collapse is prevented, CL methods can learn visual representations without negative samples saving memory and reducing computational complexity significantly. So far, these advantages have benefited many Vision Transformer-based CL methods like IBOT (Zhou J, Wei C, Wang H, et al. 2021) and DINO (Caron M, Touvron H, Misra I, et al. 2021), which exhibit superior representational ability through the global attention, scalability, and flexibility.

2.2. Contrastive Learning methods in RS

SSL methods make it possible to learn RS representations without manually annotated labels which consume a significant amount of cost. Although MIM methods, which resemble autoencoders in architecture, have been widely used to learn various RS representations, CL methods have been widely utilized in recent years due to their flexibility and global semantic learning capabilities. Stojnic et al. (2021) applied RS images to the CMC (2020). They demonstrated that even though the pre-training dataset was smaller than ImageNet, the self-supervised model trained on RGB RS images outperformed the supervised model trained on ImageNet in RS downstream tasks. Ayush K et al. (2021) and Manas O et al. (2021) utilized time-series RS images as positive sample pairs,

effectively leveraging the natural properties of time-series images for contrastive learning. However, they did not account for the potential degradation in representation quality due to land cover category changes over time. Scheibenreif L et al. (2022) and Prexl J et al. (2023) utilized medium and low resolution RS data, which are very effective for large-scale regional observations. However, they are not adequate for more general high-resolution RS surface monitoring tasks. The flexibility of CL makes it easier to take advantage of the diversity of RS data to train multimodal models by combining multiple modalities including visible, multispectral, hyperspectral, SAR, LiDAR, and so on. Jain P et al. (2022) and Wang Y et al. (2023) utilized sample pairs of multispectral and SAR images to obtain representations, while Duan P H et al. (2022) and Wang M et al. (2023) incorporated hyperspectral data and LiDAR point cloud data for pre-training. Feng Y et al. (2023) proposed a method that utilizes data distributed across multiple modalities such as visible, SAR, hyperspectral, and near-infrared. The various data modalities are modeled independently in parallel and then fused into a single backbone to obtain better results. Although these works demonstrate the adaptability of CL methods for RS data in different types, these data are expensive and difficult to obtain. In contrast, RGB remote sensing data remains the most common and available.

2.3. Semantic alignment

Contrastive Learning (CL) methods attempt to reach maximum agreement between differently augmented sample pairs. To learn semantic representations from distorted samples, CL methods tend to filter out noise introduced by augmentations and find meaningful signals in high-level features. However, positive sample pairs produced by random cropping, trying to capture features in shared regions, may sometimes have no intersection at all. Therefore, these positive sample pairs which are semantic inconsistent, can only obtain signals at low levels. Many studies have employed various methods to improve the existing pretext tasks to obtain semantically richer and more consistent positive sample pairs. LeOCLR (Alkhalefi M, Leontidis G, Zhong M. 2024) attempts to prevent inconsistencies by using the original image as anchor. SauMoCo (Kang J, Fernandez-Beltran R, Duan P, et al. 2020) and CDL (Jung H, Oh Y, Jeong S, et al. 2021) simply treat neighboring cropped images as pairs. Peng X et al. (2022) and Mishra S (2021) designed additional modules which generate proposal regions so that sample pairs are bounded within them. IndexNet (Muhtar D, Zhang X, Xiao P. 2022) and PixPro (Xie Z, Lin Y, Zhang Z, et al. 2021) attempt to learn representations through scoring mechanisms to evaluate similarity at the pixel level. Self-EMD (Liu S, Li Z, Sun J. 2020) and SCFS

(Song K, Zhang S, Luo Z, et al. 2023) utilize well-designed metrics to encourage features to learn close semantics. These improvements either fail to fully leverage the invariant semantic features in the samples or incorporate complex computations. To address these issues, we designed a straightforward method that can save memory and reach maximum semantic alignment with disjoint masks.

3. Methodology

In this section, we first present the pipeline for obtaining RS image tiles of various spatial resolutions to collect a label-free pre-training RS dataset. Then, we describe the overall approach in detail, including disjoint masks, the pre-training method, and the pixel prediction module.

3.1. Pre-training dataset

In order to achieve better generalization of the model, we designed an automatic pipeline to build an unlabeled RS pre-training dataset from internet platforms. Employing Google Earth Engine, we first collect random sample points across six continents which are demonstrated in the schematic Figure 3. In Europe, Asia and North America, where urban areas are much larger, the number of sampling points is twice that of other continents. Sampling was conducted with consideration of category boundaries defined by the ESRI 10-Meter Land Use/Land Cover map (Karra K, Kontgis C, Statman-Weil Z, et al. 2021), ensuring a diverse representation of various land cover types. Due to the significant demand for urban monitoring,

we allocated a sampling rate of 60% for urban regions and 10% each for farmland, wetlands, forests, and watersheds. In addition, we collected 1,000 sample points in each of the four regions: desert, ice, grassland, and cloud to ensure diversity. With category-balanced sample points, we download RS image tiles from online map engines Google Maps and Bing Maps. Ranging in spatial resolution from 0.3 to 10 m, these tiles have been standardized to 512×512 . Finally, we built an unlabeled pre-training remote sensing dataset with about 5 million image slices, which is called Random Sampled Remote Sensing Dataset 5m (RSRSD-5m). To the best of our knowledge, this is one of the largest publicly available unlabeled RS datasets.

Due to random sampling, slices in RSRSD-5m are quite similar to the RS images used for practical monitoring applications in industry. Unlike curated datasets that are pinpointed and filtered to obtain objects, our dataset is barely processed but rich in semantic information and data volume. We randomly sampled 100 thousand images from both well-curated dataset TOV-RS (Tao C, Qi J, Zhang G, et al. 2023) and ours, and evaluated them on the AID dataset. As shown in Table 8, even without curation, the model achieves performance comparable to that trained on curated datasets. Additionally, during formal pre-training, we incorporate the TOV dataset and the Million-AID dataset (Long Y, Xia G S, Li S, et al. 2021) to obtain more comprehensive representations in higher resolution, which are detailed in Table 1.

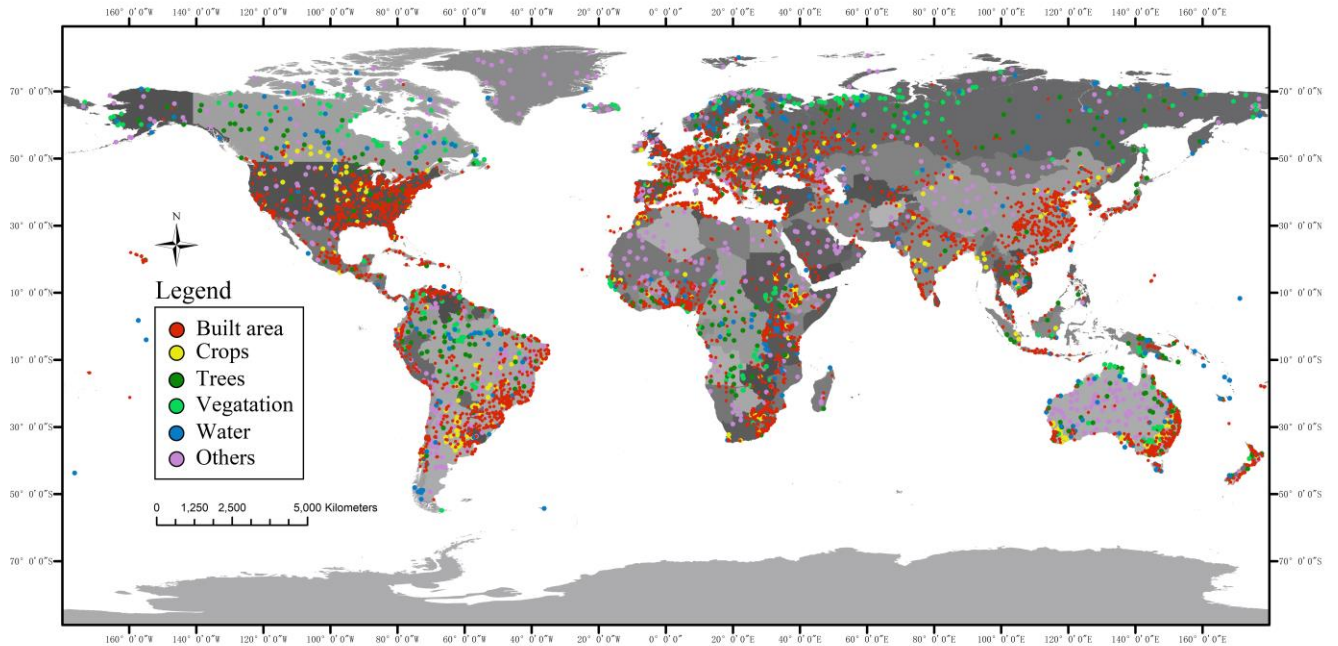


Figure 3 Illustration of global random sample points of RSRSD-5m dataset.

Table 1 Comparison among different large high-resolution RS image datasets

Dataset	Num. of Images	Spatial resolution	Source	Image Sizes
MLRSNet(2020)	109,161	0.1 to 10	Google Earth	256
Levir-KR(2021)	1,431,950	0.8 to 16	Gaofen-1, Gaofen-2, Gaofen-6	256
RSD46-WHU(2017)	117,000	0.5 to 2.4	World Map, Google Maps	256
fMoW(2018)	132,716	-	DigitalGlobe	-
Million-AID(2021)	1,000,848	0.5 to 153	Google Earth	256/512
TOV-RS(2023)	1,088,941	1 to 20	Google Earth	600
RSRSD-5m	4,686,059	0.3 to 10	Google Maps, Bing Maps	512

3.2. Pera

Our approach is designed to make all efforts to generate sample pairs that are aligned in semantics and inconsistent in appearance. To this end, we proposed an improved method that is adapted to RS, based on DINOv2 (Oquab M, Darcet T, Moutakanni T, et al. 2023). In this section, we will illustrate our method in detail in disjoint masks, pre-training method, and pixel prediction.

3.2.1. Perfectly Aligned samples

We utilize disjoint masks to obtain sparse inputs to achieve more precise and concise semantics. The overview framework of pre-training is depicted in Figure 2. As shown in Figure 2 (c), the embedded RS image x is applied with a non-overlapping mask of different ratios to divide the whole image into learnable part l , student part s and teacher part t . There is no shared areas between the three parts, and patches in part l are replaced with learnable mask tokens. The part l and the part s compose student inputs x^s , and part t composes teacher inputs x^t . Mathematically, we can define our input pair as follows:

$$x^s = sx + lm \quad (1)$$

$$x^t = tx \quad (2)$$

and we have:

$$U = s + l + t \quad (3)$$

where m denotes the learnable mask token, U denotes the universal set of the all patches, and s , t and l separately denote the masks of the student, teacher and learnable part.

3.2.2. PerA pre-training

As shown in Figure 2 (a), PerA consists of a student network and a teacher network, both networks utilize the Vision Transformer (ViT, Dosovitskiy A. 2020) as backbone network. The student contains three parts: student encoder f^s , projector g^s , and predictor q . The teacher, which has the same architecture as student only without a predictor, contains teacher encoder f^t and projector g^t . Given a sampled image $x \sim D$, we firstly apply two different augmentations t^s and t^t which contain spatial augmentations, color distortions and disjoint masks detailed in 3.2.1. The spatial augmentations in t^s and t^t , including random flipping and random resized cropping, have the same parameters to ensure spatial alignment. We follow DINOv2’s color distortion strategy, but additionally apply random grayscale. After patch embedding, we apply patchwise disjoint masks to augmented views and obtain sparse inputs $x^s = t^s(x)$ and $x^t = t^t(x)$. Containing $[cls]$ tokens $x_{[cls]}^s$, patch tokens x_p^s and learnable mask tokens x_{mask}^s , the student input x^s will be processed separately as shown in Figure 2 (b). The learnable mask tokens x_{mask}^s will participate in encoding halfway, and patch tokens x_p^s will be discarded. After encoding, the $x_{[cls]}^s$ will be processed by projector g^s to obtain projection $\hat{x}_{[cls]}^s$. The predictor q will convert learnable mask tokens x_{mask}^s to mask prediction \hat{x}_{mask}^s . Similarly, the teacher will input x^t consisting of $x_{[cls]}^t$ and x_p^t , and output a projection $\hat{x}_{[cls]}^t$. By predicting pixel

value of masked patches, the \hat{x}_{mask}^s is encouraged to reduce mean squared error (MSE) between original images. For each pixel value p_i , we have:

$$L_{MSE} = \frac{1}{B} \sum_{i=1}^B (\hat{x}_{i,mask}^s - p_i)^2 \quad (4)$$

where $\hat{x}_{i,mask}^s$ is the predicted value corresponding to each p_i . The loss function used to compute the loss for $L_{[cls]}$ can be expressed as:

$$L_{[cls]} = -H\left(\frac{t-c}{tpt_t}\right) \log\left(H\left(\frac{s}{tpt_s}\right)\right) \quad (5)$$

where t and s denote the output features of two networks, and the tpt_s and tpt_t denote the temperature values that control the sharpness of the distribution of the stent and teacher outputs. $H(\cdot)$ can be formulated as:

$$H(\cdot) = \frac{\exp(\cdot)}{\sum_{k=1}^K \exp(\cdot)} \quad (6)$$

Given a momentum n , c updates with the batch mean of the teacher's output to reduce the probability of model collapse, which the formula can express as:

$$c \leftarrow nc + (1-n) \frac{\sum_{b=1}^B \hat{x}_{b,[cls]}^t}{B} \quad (7)$$

where B denotes the batch size and $\hat{x}_{b,[cls]}^t$ denotes every teacher output projection in the batch. Additionally, we incorporate the Kolo loss to encourage dispersion of the output feature vectors in the embedding space and prevent potential model collapse. The formula for the KoLeo loss is as follows:

$$L_{Kolo} = -\frac{1}{B} \sum_{i=1}^B \log(\|x_i - x_{i'}\|_2 + \varepsilon) \quad (8)$$

where B denotes the batch size, $\|x_i - x_{i'}\|_2$ denotes the euclidean distance between features and ε is a constant. The student network updates the weights by backpropagating, following the weighted-sum loss function:

$$L = C_1 L_{[cls]} + C_2 L_{MSE} + C_3 L_{Kolo} \quad (9)$$

where C_1 , C_2 , and C_3 are weighting constants, empirically assigned values of 1.0, 0.1, and 0.01, respectively.

Distinct from the student, the teacher updates using an exponential moving average (EMA) with momentum m , which can delineated as:

$$\theta_t \leftarrow m\theta_t + (1-m)\theta_s \quad (10)$$

where θ_s and θ_t denote student and teacher weights. The momentum m is usually large, ranging in $[0, 1]$ to ensure that the teacher weights θ_t can be updated slowly.

3.2.3. Downstream transferring

The transfer learning technique helps the model to achieve better performance in the target domain by transferring the knowledge learned by pre-training. Aiming to learn a representation that can easily transfer to various

downstream tasks, we employ the teacher encoder as the backbone and concatenate it with task-specific heads. However, the Vision Transformer is trained on sequential data and lacks the spatial priors inherent in convolutional neural networks. This limitation makes ViT perform poorly on dense prediction tasks. To address this issue, we utilize ViT-Adapter (Chen Z, Duan Y, Wang W, et al. 2022) to enhance performance on dense prediction tasks, such as segmentation. As shown in Figure 2 (d), we use the original teacher encoder in classification, whereas for dense prediction tasks, we warp the encoder with ViT-Adapter to capture more spatial information.

4. Experiments

To evaluate the performance of our proposed PerA, we first introduce our pre-training implementation setting in detail. Next, we conduct experiments on scene classification, semantic segmentation and change detection. At the end of the section, we present detailed ablation experiments and feature visualizations. All experiments were implemented with NVIDIA A100 40G GPUs.

4.1. Pre-training implementation

We utilized ViT as the backbone and pre-trained the model on our unlabeled pre-training dataset, which was described in detail in 3.1. By default, we employed the AdamW optimizer (Loshchilov I, Hutter F. 2017) with a batch size of 192. We conducted pre-training on a slim ViT-G/16-1024 model with an embedding dimension of 1024 and 505M parameters for 200 epochs. The learning rate is linearly ramped up during the first 20 epochs to its base value and then decayed with a cosine schedule after warmup. The weight decay and the momentum m also follow the cosine schedule but slowly increase throughout the pre-training. The student temperature is set to a constant value of 0.1. In contrast, the teacher temperature grows linearly to a maximum value in the first 30 epochs and remains constant until the end of pre-training. We utilized a large number of head prototypes, specifically 131,072, and a high drop path rate of 0.3. The student and teacher mask ratios were set to 0.3 and 0.5, with the remaining 0.2 allocated to the learnable portion. For image augmentations, we adopted multi-crop, random flipping, random resized cropping, followed by color distortion consisting of a random sequence of brightness, contrast, saturation, hue adjustments, and a grayscale conversion.

4.2. Downstream tasks performance

We employed the encoder-decoder paradigm to adapt the learned representations to a specific task, as explained in 3.2.3. We evaluate our model on the AID dataset (Xia G S, Hu J, Hu F, et al. 2017), UC Merced dataset (Yang Y, Newsam S. 2010), ISPRS Potsdam dataset (Sherrah J. 2016), LoveDA dataset (Wang J, Zheng Z, Ma A, et al.

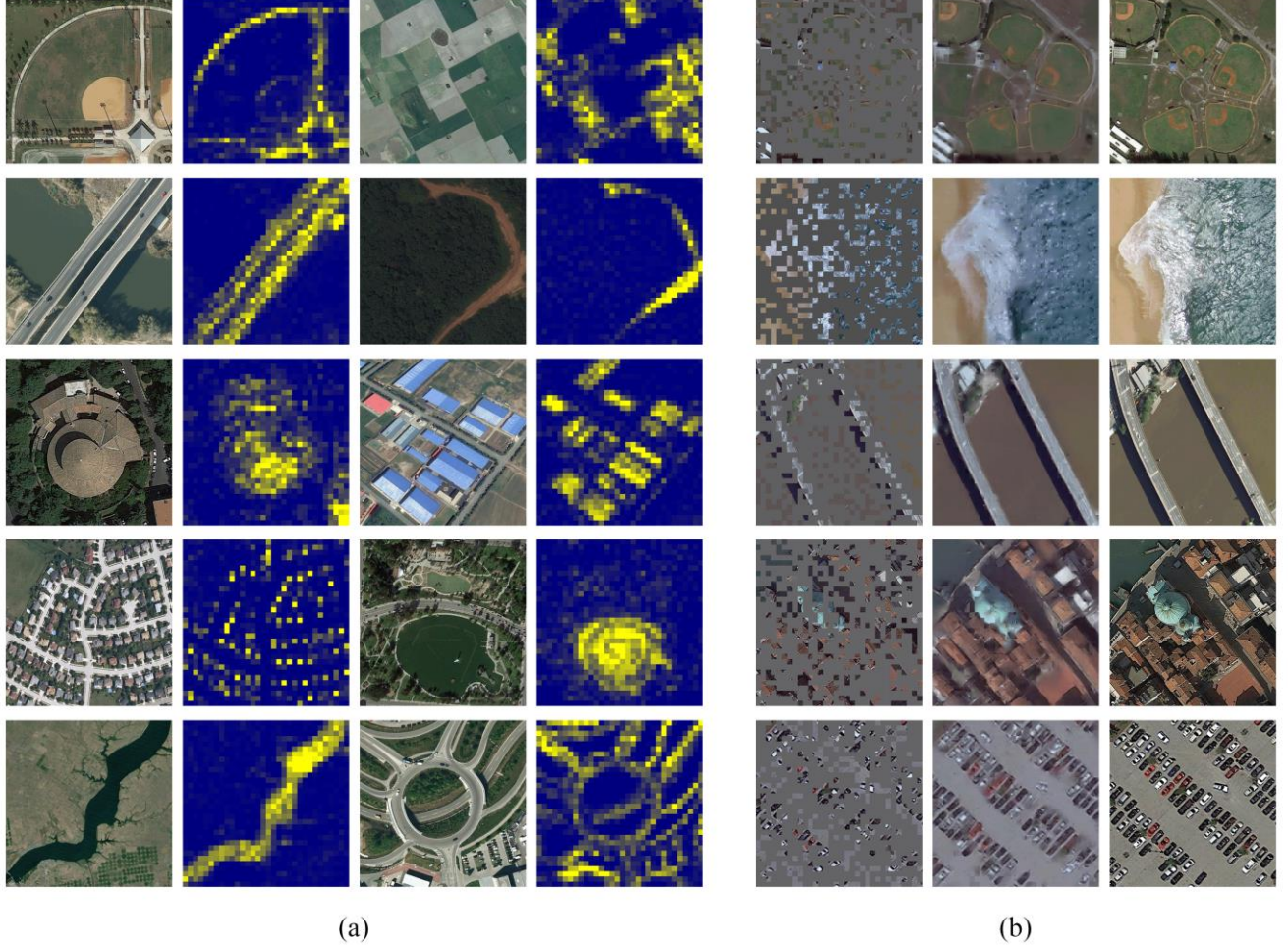


Figure 4. Self-attention maps and reconstruction maps with 16×16 patches on AID dataset. All the images are not used during pre-training. (a) For each pair, we show the ground-truth (left) and self-attention map (right); (b) For each triplet, we show masked image (left), reconstruction map (middle) and ground-truth (right).

2021), LEVIR-CD dataset (Chen H, Shi Z. 2020) and DIOR dataset (Li K, Wan G, Cheng G, et al. 2020), which are representative RS datasets for scene classification, semantic segmentation, change detection, object detection, respectively. The results indicated that our model achieved performance comparable to previous state-of-the-art methods with a limited model scale, demonstrating the effectiveness and generalization capability of our method.

4.2.1. Scene classification

For scene classification, we evaluate our model on AID dataset and UC Merced dataset. We first introduce these datasets in detail:

AID dataset: AID dataset is a large-scale dataset for aerial scene classification. Consisting 10,000 high-resolution aerial images ranging in 0.5 to 8 m, these images are standardized to a size of 600×600 and are divided into 30 categories. The dataset is designed to have

high intra-class diversity and low inter-class dissimilarity making classification more challenging.

UC Merced dataset: UC Merced scene classification dataset (UCM) is a standard dataset widely used in RS image scene classification which contains 2,100 high-resolution RS images. These image tiles consist of 21 land-use classes derived from aerial orthoimagery with a pixel resolution of one foot. All these images are downloaded from United States Geological Survey (USGS) National Map of 20 regions of United States. In each class, the dataset contains 100 images in size of 256×256 and all of them were carefully selected to prevent homogeneity.

Implementation Details: We utilized linear classifier to transfer our pre-trained model to domain of the dataset. For each dataset, all the images are resized to 512×512 before scene classification. For AID dataset, we divide the dataset into training and test sets in a ratio of 2

Table 2 Comparisons with other RS foundation models on AID dataset.

Method	Arch.	AID TR=20%
		OA
RSP(2022)	ViTAEv2-S	96.91
RVSA(2022)	ViTAE-B	97.03
Scale-MAE(2023)	ViT-L	96.44
SeCo(2021)	ResNet-50	93.47
SatMAE(2022)	ViT-L	95.02
TOV(2023)	ResNet-50	95.16
CMID(2023)	Swin-B	96.11
GASSL(2021)	ResNet-50	93.55
SSL4EO(2023)	ViT-S	91.06
CACo(2023)	ResNet-50	90.88
SatLas(2023)	Swin-B	94.96
GFM(2023)	ViT-L	95.47
Skysense(2024)	ViT-L + Swin-H	97.68
Ringmo(2022)	Swin-B	96.90
PerA	ViT-G/16-1024	97.13

to 8 according Sun X, Wang P, Lu W, et al. (2022). We finetuned the model with AdamW optimizer and Cross Entropy Loss for 200 epochs. The batch size was set to 16, and weight decay was set to $5e-6$. The learning rate was ramped up to its maximum value $1e-4$ during the initial 20 epochs, and then it is gradually decreased using a cosine scheduler. For the UCM dataset, we employed an 8:2 training-test split based on Sun X, Wang P, Lu W, et al. (2022) and a 5:5 split based on Wang D, Zhang Q, Xu Y, et al. (2022). Unlike the AID experiments, we set the learning rate and the weight decay to $5e-5$ and $1e-4$. We set the drop path rate to 0.3 to enhance the model’s generalization ability. For data augmentations, we used random flipping, random cropping and color distortion.

Results and Analyses: We evaluate our pre-trained model’s capabilities through fine-tuning performance and report overall accuracy (OA). As shown in Table 2, we compared the finetuning performance with other RS foundation models on AID dataset. We note that our model can reach the best level with a limited model scale even though we used only 20% of the data as the training set which proves the effectiveness of our method. On the other hand, as shown in Table 3, under the commonly used 80% training data setting, our model achieved up to 100% overall accuracy on the test set of UCM dataset. Although such results are partly influenced by randomness and do not prove that the finetuned model can fully fit the entire dataset, they still demonstrate the strong scene classification capability of our pre-trained model. Given the relatively low complexity of the task setting, we additionally conducted experiments utilizing 50% training

Table 3 Comparisons with other RS foundation models on UC Merced dataset.

Method	UCM TR=50%	UCM TR=80%
	OA	OA
RSP(2022)	99.62	99.90
GeoKR(2021)	95.49	-
GeCo(2022)	96.32	-
SeCo(2021)	-	97.86
CMID(2023)	-	99.48
RVSA(2022)	99.70	-
Ringmo(2022)	-	99.84
PerA	99.71	100.0

data and compared our model with several other existing RS pre-training methods. Our model still achieved the best performance that demonstrate the superiority of our proposed method.

4.2.2. Semantic segmentation

We conducted experiments on ISPRS Potsdam dataset and LoveDA dataset, which are RS datasets for semantic segmentation widely utilized to evaluate the dense prediction ability of models. The datasets are introduced as following:

ISPRS Potsdam dataset: The Potsdam dataset contains 38 high resolution aerial images within 0.5 m, and all of them are 6000×6000 pixels in size. The dataset was obtained in Potsdam city, Germany, which contains large building blocks, narrow streets and dense settlement structure. The dataset has six categories of labels in dataset, including impervious surfaces, building, low vegetation, tree, car, and clutter. The dataset also provides near infrared band imagery and digital surface models (DSMs). However, we only utilized RGB optical data for segmentation task.

LoveDA dataset: The LoveDA dataset consists of 2,522 training, 1,669 validation, and 1,796 test images. The dataset was obtained from Nanjing, Changzhou and Wuhan city in China through Google Earth platform. Each image has fixed pixel size of 1024×1024 and 0.3 spatial resolution. The dataset includes seven classes: buildings, roads, water, barren land, forests, agriculture, and background. The images are sampled in both urban and rural areas using different data collection strategies to increase its diversity and difficulty.

Implementation Details: The models are finetuned with ViT-Adapter to enhance performance on dense prediction tasks as described in 3.2.3. The UPerNet (Xiao T, Liu Y, Zhou B, et al. 2018) was employed to capture multi-level spatial features. We applied its decoder to our pre-trained backbone. In UPerNet decoder, we set hidden channels to 512 and output channels to 256. For Potsdam

Table 4 Comparisons with other RS foundation models on Potsdam dataset.

Method	Arch.	Potsdam mF1
RSP(2022)	ViTAEv2-S	90.64
RVSA(2022)	ViTAE-B	91.22
Scale-MAE(2023)	ViT-L	91.54
SeCo(2021)	ResNet-50	89.03
SatMAE(2022)	ViT-L	90.63
TOV(2023)	ResNet-50	92.03
CMID(2023)	Swin-B	91.86
GASSL(2021)	ResNet-50	91.27
SSL4EO(2023)	ViT-S	91.54
CACo(2023)	ResNet-50	91.35
SatLas(2023)	Swin-B	91.28
GFM(2023)	ViT-L	91.85
Skysense(2024)	ViT-L + Swin-H	93.99
Ringmo(2022)	Swin-B	91.27
PerA	ViT-G/16-1024	93.08

dataset, we separated the 38 images into a training set of 24 images and a test set of 14 images following the setting of previous works. All the images were cropped into 512×512 , and we overlapped them when it is out of boundary. We finetuned our model for 200 epochs with AdamW optimizer, Cross Entropy Loss, and batch size of 8. The learning rate would increase from 0 to $1e-4$ in 20 initial epochs, and slowly decrease to $5e-6$. The drop path rate was set to 0.1, and the weight decay was set to $1e-4$. We only adopted random flipping and random resized cropping for augmentations. For LoveDA dataset, we utilized official splits to finetune our model. Since the ground truth labels of the test set were not provided, we uploaded the inference results to the official evaluation server¹. We set the maximum learning rate to $5e-5$, while keeping the other settings the same as those used in the experiments on the Potsdam dataset.

Results and Analyses: We reported mean F1-score of experiment results on Potsdam dataset. As shown in Table 4 compared with other methods, our method can achieve competitive segmentation capability on the Potsdam dataset. Under the same experiment setting, our model outperformed the majority of existing pre-training methods and achieved less than a 1% difference in the mF1 metric compared to the current state-of-the-art, despite having a significantly smaller model size and pre-training data scale. For LoveDA dataset, we estimate the performance of our model using mean intersection over union (mIoU). As shown in Table 5, our method achieved a 54.02% mIoU on the test set of the LoveDA dataset. Although it does not surpass the current state-of-the-art

Table 5 Comparisons with other RS foundation models on LoveDA dataset.

Method	Arch.	LoveDA mIoU
RSP(2022)	ViTAEv2-S	53.02
SeCo(2021)	ResNet-50	44.64
BFM(2023)	ViT-G/12	54.40
RVSA(2022)	ViTAE-B	52.44
CACo(2023)	ResNet-50	48.89
TOV(2023)	ResNet-50	49.70
GeRSP(2024)	ResNet-50	50.56
Geo-Aware(2019)	ResNet-50	49.37
MTP(2024)	ViT-L + RVSA	54.17
SelectiveMAE(2024)	ViT-L	54.31
GASSL(2021)	ResNet-50	48.76
PerA	ViT-G/16-1024	54.02

result, it still ranks among the top-performing pre-training methods.

4.2.3. Change detection

Change detection plays a crucial role in land use monitoring, environmental protection, and disaster response. With the growing emphasis on change detection tasks, the ability of remote sensing foundation models to perform change detection has become an important indicator for evaluating their overall capability. For change detection, we adopted LEVIR-CD to evaluate our method. In the following, we provide a detailed introduction to the LEVIR-CD dataset:

LEVIR-CD dataset: The LEVIR-CD dataset, a high-resolution building change detection dataset, consists of 445, 64, and 128 pairs of RS images each in the training, validation, and test sets. The images were captured in Texas state, USA, including Austin, Lakeway, Bee Cave, Buda, Kyle, Manor, Pflugervilletx, Dripping Springs, etc., between 2002 and 2018. Each image is 1024×1024 pixels in size. All of the temporal RS images in the dataset are in a spatial resolution of 0.5m. Additionally, the seasonal changes and the illumination changes are also introduced to the dataset, which make it more difficult to interpreting.

Implementation Details: For change detection tasks, we combined our encoder with BIT head (Chen H, Qi Z, Shi Z. 2021), and finetuned it for 500 epochs. We retained the original parameters of the BIT model, and simply replace the ResNets to our pre-trained encoders. Same as general change detection approaches, the backbone preforms two forward passes and shares the same weight in both. The LEVIR-CD dataset provides standard training, validation, and test sets. Following common practices in existing methods Sun X, Wang P, Lu W, et al. (2022), we cropped all image tiles into samples of 512×512 pixels. We finetuned our model with pixel-level Cross Entropy

¹<https://codalab.lisn.upsaclay.fr/competitions/421>

Table 6 Comparisons with other RS foundation models on LEVIR-CD dataset.

Method	Arch.	LEVIR-CD
		F1
RSP(2022)	ViTAEv2-S	90.93
RVSA(2022)	ViTAE-B	90.86
Scale-MAE(2023)	ViT-L	92.07
SeCo(2021)	ResNet-50	90.14
SatMAE(2022)	ViT-L	87.65
CMID(2023)	Swin-B	91.72
GASSL(2021)	ResNet-50	78.19
SSL4EO(2023)	ViT-S	89.05
CACo(2023)	ResNet-50	81.04
SatLas(2023)	Swin-B	90.62
GFM(2023)	ViT-L	91.73
Skysense(2024)	ViT-L + Swin-H	92.58
Ringmo(2022)	Swin-B	91.86
PerA	ViT-G/16-1024	92.34

Loss and AdamW optimizer. The batch size was set to 8, and the drop path rate was set to 0.2. After the learning rate climbs to $1e-4$, it will decrease to $1e-6$ following a cosine scheduler. We adopted random flipping and random resized cropping for augmentations and disabled all color jittering.

Results and Analyses: We evaluate the change detection capability of our model on LEVIR-CD dataset, and report the F1 score of the foreground class in the prediction results. The model’s performance is available in Table 6, and we notice that our model can achieve competitive result of 92.34% F1 score. The result outperforms most existing RS pre-trained models and exhibits a marginal gap of only 0.24% compared to the state-of-the-art performance, which demonstrates the superiority of our approach in the change detection task.

4.2.4. Object detection

Object detection tasks focus on identifying and localizing specific categories of objects, and play a critical role of urban planning, traffic monitoring, maritime surveillance, and disaster response. Unlike natural image object detection, RS object detection tasks often deal with challenges such as varying scales, complex backgrounds, small object sizes, and diverse imaging conditions, making it more challenging to RS interpreting. For object detection, we conducted experiments on extensively utilized DIOR dataset to evaluate the object detection performance of our model. The following is a detailed introduction to the DIOR dataset:

DIOR dataset: The DIOR dataset is a large -scale public RS object detection dataset, that contains 20 common RS object categories, including Airplane, Ship, Overpass, Wind mill, Chimney, Harbor, Stadium Vehicle,

etc. Captured on Google Earth platform, all the images have a size of 800×800 pixels and spatial resolutions ranging from 0.5m to 30m. The dataset provides official splits of trainval set and testing set that contain 11,725 images and 11,738 images. The objects in dataset a large range of object size variations, not only in terms of spatial resolutions, but also in the aspect of inter- and intra-class size variability across objects. The diversity and broad coverage of the dataset present significant challenges for the RS object detection task.

Implementation Details: We utilized the Faster R-CNN (Ren S, He K, Girshick R, et al. 2015) like previous SSL works, and assembled it with our pre-trained RS encoder. We employed the official implementation from Pytorch and adjusted several parameters to better accommodate the characteristics of object detection in RS scenarios. We set anchor sizes to a range of 4 to 512 to capture more tiny objects like cars and ships, and set aspect ratios to a range of 0.2 to 5.0 to fit some slim targets. The RPN NMS threshold was set to 0.8, box score threshold was set to 0.01, and the detections for images were set to 200. All the images are resized to sizes of 512×512 online, and the bounding boxes are also rescaled according to the images. We finetuned and evaluated our model with AdamW optimizer for 100 epochs on the official splits. The batch size was set to 16 and the weight decay was set to $1e-3$. The learning rate was set to $1e-4$, and after warming up, it decreased according the cosine scheduler. We set the drop path rate to 0.3 to enhance the model’s generalization ability. For data augmentations, we used random flipping and color distortion.

Results and Analyses: We finetuned our pre-trained RS foundation model on DIOR dataset to evaluate the object detection ability of our method and report mAP_{50} metric. As shown in Table 7, our method achieved 75.71%

Table 7 Comparisons with other RS foundation models on DIOR dataset.

Method	Arch.	DIOR
		mAP_{50}
RVSA(2022)	ViTAE-B	73.22
Scale-MAE(2023)	ViT-L	73.81
SatMAE(2022)	ViT-L	70.89
TOV(2023)	ResNet-50	70.16
CMID(2023)	Swin-B	75.11
GASSL(2021)	ResNet-50	67.40
SSL4EO(2023)	ViT-S	64.82
CACo(2023)	ResNet-50	66.91
SatLas(2023)	Swin-B	74.10
GFM(2023)	ViT-L	72.84
Skysense(2024)	ViT-L + Swin-H	78.73
PerA	ViT-G/16-1024	75.71

mAP₅₀ on DIOR dataset. Although this result surpasses the majority of existing RS pre-training methods, there remains a performance gap compared to the current state-of-the-art. This discrepancy may be attributed to the global attention mechanism of the Vision Transformer (ViT), which, despite the introduction of spatial information via the ViT-Adapter, still lacks the inherent spatial priors present in architectures such as the Swin Transformer. Future work could further investigate and refine this aspect to enhance performance.

4.3. Comparative results

4.3.1. Comparison on uncured data

A series of comparative experiments were conducted on uncured data. As depicted in Table 8, we pre-trained ViT-B with PerA and DINO V2 method on sampled pre-training dataset TOV-100k and RSRSD-100k. Unlike curated TOV dataset, the images in RSRSD dataset are not restricted to specific target locations and closer to the characteristics of the data in practical interpreting tasks while easier to access. The PerA method extracts precise and concise semantics from sparse inputs which enable the model to be pre-trained in arbitrarily cropped RS images avoiding semantic inconsistency. We performed scene classification tasks on AID dataset to verify our conclusion. The experimental results indicate that, under identical experimental conditions, our method PerA obtained similar performance on both curated and uncured datasets, whereas baseline method DINO V2 exhibited significant performance degradation when applied to uncured data. These experimental results demonstrate the superior robustness of our method and its enhanced capability in conducting pre-training with uncured data. Furthermore, the experiments indirectly validate our method's effectiveness in reducing semantic inconsistency issues, as uncured data presents a higher probability of semantic inconsistency occurrences due to scattered distribution. This remarkable adaptability to uncured data can be attributed to the specially designed pretext task in our method, which enhances the semantic alignment of sample pairs for scattered geospatial objects while reducing the model's reliance on the spatial distribution of objects in the data.

4.3.2. Comparison with other SSL methods

We evaluate semantic learning capability between different SSL methods in same setting. All experiments were performed using the ViT-B backbone with different approaches, including both CL and MIM. We pre-trained all these models on TOV-100k for 200 epochs and conducted downstream experiments on the AID dataset. As shown in Table 9, we report overall accuracy of AID dataset. Under the same experimental setting, our method achieves the best performance among a number of

Table 8 Comparison of results using uncured data.

Method	Arch.	Data	AID TR=20%
			OA
PerA	ViT-B	TOV-100k	90.1
		RSRSD-100k	90.0
DINO V2	ViT-B	TOV-100k	82.3
		RSRSD-100k	79.3

advanced SSL methods including CL and MIM. The results demonstrate the potential of our pre-training method for semantic understanding of RS images and prove the effectiveness of combination CL and MIM methods.

Furthermore, we conduct comparisons of computational resource between different CL methods which have a similar structure. All the models are pre-trained with ViT-B on TOV-100k dataset. The images in dataset were cropped into 512×512 , and batch size was set to 16. Resource usage information such as computational complexity and memory consumption is reported in Table 10. The result shows that, comparing with other CL methods, our method provides dramatic improvements in training speed, computational complexity, and memory consumption. Thanks to the reduction in redundant information from the sparse input, our method reduces image processing time to about half, and memory usage to approximately one-quarter, compared to the baseline approach DINO V2. The results indicate that our approach enables pretraining with lower resource consumption while still achieving strong performance.

Table 9. Comparison of the performance of different SSL methods under the same settings.

Method	Arch.	Type	AID TR=20%
			OA
DINO		CL	80.1
MAE		MIM	84.9
MoCo V3	ViT-B	CL	69.2
DINOv2		CL	82.3
PerA		CL	90.1

Table 10. Comparison of the resource usage of different SSL methods under the same settings.

Method	im/s	GFLOPs	epoch time	GPU Mem
DINO	33.90	1177.58	49m15s	24.82G
MoCo V3	50.72	351.05	32m55s	11.55G
DINO V2	69.28	1249.93	24m56s	26.16G
PerA	112.69	146.85	14m49s	6.64G

4.4. Ablation studies

4.4.1. Performance improvement

Based on DINO V2 framework, PerA implemented a series of performance optimizations and component improvements. These performance improvements are well demonstrated under combinations of the components. By introducing components progressively, we conducted comparative analysis of our method's performance on the AID dataset. As shown in Table 11, we pre-trained models integrated from different components on TOV-100k for 200 epochs. Initially, we discarded IBOT patch-level alignment since the asymmetric design of our method learns between sample pairs with no shared regions, which would lead to IBOT failure. After applying spatial alignment, the model's performance was diminished due to spatial correspondence issues, as overly simplistic samples hinder its ability to learn high-level semantic features. However, when disjoint masks were introduced, the challenging pretext tasks helped restore the accuracy to normal levels — or even improve it further. Building on this, the pixel prediction significantly improved the semantic capabilities of the model, resulting in an overall accuracy of 90.1%. Additionally, we evaluate our approach without spatial alignment, which indicates that the improvements are the result of the combined effects of spatial alignment, sparse input and pixel prediction.

4.4.2. Ablation studies of different patch sizes

According to the theory behind our method, using the smallest possible patch size can eliminate semantic inconsistency. However, the actual impact of patch size in experiments is more complex. Extremely small patch sizes significantly increase computational cost while also reducing the difficulty of the pre-text task, leading to performance degradation.

Several experiments were conducted with different patch sizes to evaluate the impact of patch size on model performance. We pre-trained models on TOV-100k for

Table 11. Ablation studies of the different improvements with ViT-B. SA: spatial alignment; DM: disjoint mask; PP: pixel prediction.

Method	IBOT	SA	DM	PP	AID TR=20% OA
DINOv2	√				81.4
PerA		√			75.7
		√	√		84.9
			√	√	89.6
		√	√	√	90.1

Table 12. Performance on AID dataset for different patch sizes.

Method	Arch.	Patch size	AID TR=20% OA
		16	90.1
PerA	ViT-B	14	90.5
		8	89.3

200 epochs. As shown in Table 12, all these experiments were in same settings, and we report the differences in results under different patch size configurations. We can observe that the model's performance improves when the patch size is reduced from 16 to 14, which is consistent with the general behavior of ViT. However, when patch size was set to 8, potential agent task simplification leads to a noticeable decay in model performance.

4.4.3. Ablation studies on different mask ratios

The disjoint masks divide each input RS image into three parts: the student part (s), the learnable part (l), and the teacher part (t). The ratio of disjoint mask is a sensitive hyperparameter in our method. Through extensive experiments, we found that the pre-trained model performs optimally when t ratio is set to 50% or 60%. The pre-training performs best when the ratio between the s part and the l part is approximately 1:1. Although the pixel information in the l part is masked, it can still be implicitly captured through the reconstruction target. We conducted more detailed experiments to find best ratios of disjoint mask, which are presented in Table 13.

Table 13. Ablation studies of different mask ratios

Method	<i>s</i> ratio	<i>l</i> ratio	<i>t</i> ratio	AID TR=20%
				OA
PerA	30%	20%	50%	91.4
	20%	30%	50%	91.9
	20%	20%	60%	91.9
	30%	10%	60%	90.7

4.5. Visual Analysis

We conducted several visual analysis experiments to interpret the improvements introduced by our method and to demonstrate its advantages.

4.5.1. Attention maps and reconstruction

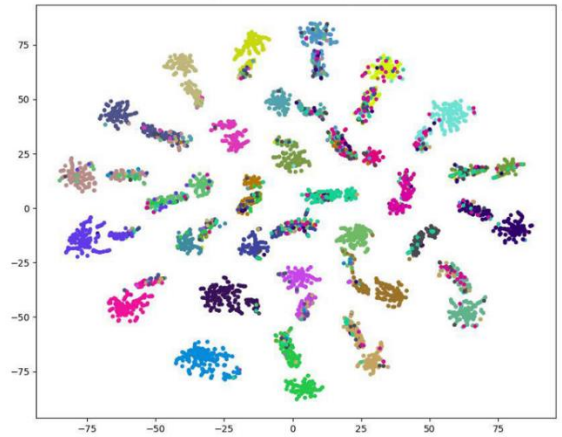
We performed several visualizations of the pre-trained model and identified that the model pre-trained by our method shares the specific properties of both CL and MIM. Due to unique architecture that combines CL method with MIM method, PerA possesses distinctive properties that are not found in other methods. As shown in Figure 4 (a), similar to the CL method DINO, the encoder pre-trained with PerA produces semantic-rich attention maps that clearly delineate the boundaries of objects in RS images. In each image pair, the left image is the original image from AID dataset, while the right image shows the attention map obtained from pre-trained PerA encoder. The attention maps are generated from the multi-head attention module of ViT, where each attention head can capture different semantic features. Sometimes, the objects in these maps are so precise and that even comparable to those produced by segmentation methods. Since the AID dataset was not involved during pre-training, these attention maps are obtained under a fully zero-shot situation, which demonstrates the strong semantic understanding ability of our method based on perfectly aligned sample pairs.

Moreover, due to the incorporation of the pixel reconstruction mechanism, the model pre-trained by PerA also exhibits powerful pixel reconstruction capability which is usually associated with MIM methods. As illustrated in Figure 4 (b), the pre-trained encoder with its prediction head can accurately reconstruct heavily masked input RS images. For each triplet of images, the left image is the masked input, the center image is the reconstructed output, and the right image is the original RS image. These pixel reconstruction predictions are also conducted on the AID dataset, which was not involved during pre-training. The fact that the pre-trained model can almost perfectly reconstruct images with up to 70% masking, without any

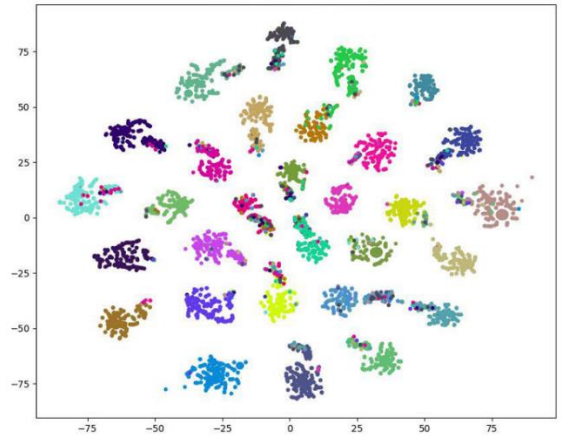
prior knowledge of the dataset, further demonstrates its deep understanding of both image structure and semantics. This shows that the model can understand sparse input information and transfer them into essential, semantic-rich features, while maintaining strong robustness to noise.

4.5.2. t-SNE visualization

We conducted t-SNE visualization of the feature distributions produced by the baseline method DINO V2 and the improved method PerA on AID dataset, clearly demonstrating the improvement in semantic representation achieved by our approach. As presented in Figure 5, all classified features are downscaled and visualized as scatter plots in feature space. In the plots, each color represents a different category. It can be observed that our method achieves significant improvement over the baseline in terms of intra-class compactness, with a noticeable reduction in misclassified feature points within each class. This intuitively reflects the improved classification capability of the proposed method on downstream tasks.



(a) t-SNE map of DINO v2



(b) t-SNE map of PerA

Figure 5 Comparison of t-SNE maps of (a) DINOv2 and (b) PerA.

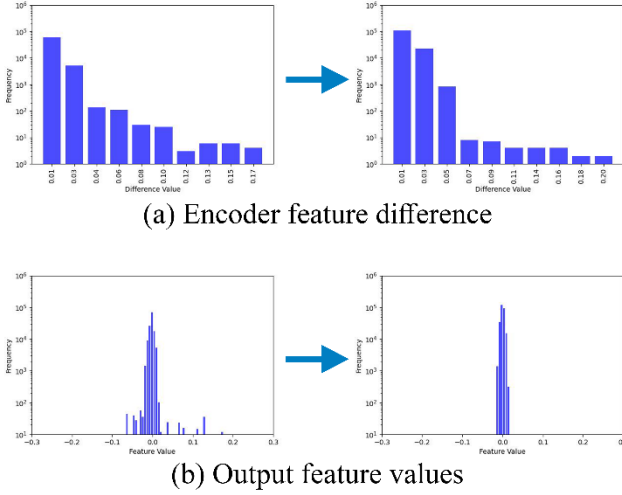


Figure 6. (a) Comparison of output feature differences between student and teacher encoders across methods (b) Comparison of the output feature distribution across different methods.

4.5.3. Feature histogram

To further analyze what is the difference of representations between our improved method and baseline, we conducted histogram visualizations for pre-trained encoder feature outputs. As depicted in Figure 6 (a), we computed the output feature differences between student and teacher encoder across our improved method and baseline method DINO V2. The histograms reflect a noticeable increase in the frequency of lower difference values and a corresponding decrease in the frequency of higher values. These statistical results indicate that the improved method leads to a significantly reduced feature differences between the teacher and student networks and a better high-level semantic understanding.

Additionally, as shown in Figure 6 (b), we compared output feature distributions of pre-trained model between DINO V2 and PerA. In the histograms of feature distribution, our method exhibited a more pronounced peak and a significant reduction in the discrete values. The contraction of the feature range, accompanied by improved downstream task performance, suggests that the model has learned more generalizable and high-level features from sparse inputs, effectively discarding redundant information.

5. Conclusion

In this paper, we proposed a contrastive learning pre-training method named PerA which is designed to adapt RS images. PerA is intended to generate sample pairs with as consistent semantics as possible while maximizing the utilization of the samples. Compared with other RS unlabeled pre-training models, our method obtained

remarkable performance on several downstream tasks with a limited model scale. We also present an unlabeled RS pre-training dataset called RSRSD-5m, which contains about 5 million RS images. To the best of our knowledge, this is one of the largest publicly available unlabeled RS datasets. In the future, we aim to reduce the cost of using models through methods such as knowledge distillation, enabling its better application in practical remote sensing monitoring tasks.

Disclosure statement

No potential conflict of interest was reported by the authors.

Funding

This work was supported by the [National Key R&D Program of China] under Grant [number 2023YFB3907600] and [Chinese Academy of Surveying and Mapping Fundamental Research Funds] under Grant [number AR2420].

Data availability statement

The source code, weights, and datasets are available at <https://github.com/SathShen/PerA>.

References

- Pei T, Xu J, Liu Y, et al. GIScience and remote sensing in natural resource and environmental research: Status quo and future perspectives[J]. *Geography and Sustainability*, 2021, 2(3): 207-215.
- Chen Y, Fan R, Yang X, et al. Extraction of urban water bodies from high-resolution remote-sensing imagery using deep learning[J]. *Water*, 2018, 10(5): 585.
- Nguyen T T, Hoang T D, Pham M T, et al. Monitoring agriculture areas with satellite images and deep learning[J]. *Applied Soft Computing*, 2020, 95: 106565.
- Yuan Q, Shen H, Li T, et al. Deep learning in environmental remote sensing: Achievements and challenges[J]. *Remote sensing of Environment*, 2020, 241: 111716.
- Reed C J, Gupta R, Li S, et al. Scale-mae: A scale-aware masked autoencoder for multiscale geospatial representation learning[C]//*Proceedings of the IEEE/CVF International Conference on Computer Vision*. 2023: 4088-4099.
- Stojnic V, Risojevic V. Self-supervised learning of remote sensing scene representations using contrastive multiview coding[C]//*Proceedings of the IEEE/CVF Conference on Computer Vision and Pattern Recognition*. 2021: 1182-1191.
- Geiping J, Garrido Q, Fernandez P, et al. A Cookbook of Self-Supervised Learning[J]. *arXiv preprint arXiv:2304.12210*, 2023.

- Chen X, Xie S, He K. An empirical study of training self-supervised vision transformers[C]//Proceedings of the IEEE/CVF international conference on computer vision. 2021: 9640-9649.
- Muhtar D, Zhang X, Xiao P. Index your position: A novel self-supervised learning method for remote sensing images semantic segmentation[J]. IEEE Transactions on Geoscience and Remote Sensing, 2022, 60: 1-11.
- Jean N, Wang S, Samar A, et al. Tile2vec: Unsupervised representation learning for spatially distributed data[C]//Proceedings of the AAAI Conference on Artificial Intelligence. 2019, 33(01): 3967-3974.
- Wang D, Zhang J, Du B, et al. An empirical study of remote sensing pretraining[J]. IEEE Transactions on Geoscience and Remote Sensing, 2022, 61: 1-20.
- Wang T, Isola P. Understanding contrastive representation learning through alignment and uniformity on the hypersphere[C]//International conference on machine learning. PMLR, 2020: 9929-9939.
- Ji W, Deng Z, Nakada R, et al. The power of contrast for feature learning: A theoretical analysis[J]. Journal of Machine Learning Research, 2023, 24(330): 1-78.
- Wen Z, Li Y. Toward understanding the feature learning process of self-supervised contrastive learning[C]//International Conference on Machine Learning. PMLR, 2021: 11112-11122.
- Muhtar D, Zhang X, Xiao P, et al. Cmid: A unified self-supervised learning framework for remote sensing image understanding[J]. IEEE Transactions on Geoscience and Remote Sensing, 2023, 61: 1-17.
- Li Y, Xie S, Chen X, et al. Benchmarking detection transfer learning with vision transformers[J]. arXiv preprint arXiv:2111.11429, 2021.
- Zhou Q, Yu C, Luo H, et al. Mimco: Masked image modeling pre-training with contrastive teacher[C]//Proceedings of the 30th ACM International Conference on Multimedia. 2022: 4487-4495.
- Huang Z, Jin X, Lu C, et al. Contrastive masked autoencoders are stronger vision learners[J]. IEEE Transactions on Pattern Analysis and Machine Intelligence, 2023.
- Bromley J, Guyon I, LeCun Y, et al. Signature verification using a " siamese " time delay neural network[J]. Advances in neural information processing systems, 1993, 6.
- Wu Z, Xiong Y, Yu S X, et al. Unsupervised feature learning via non-parametric instance discrimination[C]//Proceedings of the IEEE conference on computer vision and pattern recognition. 2018: 3733-3742.
- Tian Y, Krishnan D, Isola P. Contrastive multiview coding[C]//Computer Vision–ECCV 2020: 16th European Conference, Glasgow, UK, August 23–28, 2020, Proceedings, Part XI 16. Springer International Publishing, 2020: 776-794.
- Chen T, Kornblith S, Norouzi M, et al. A simple framework for contrastive learning of visual representations[C]//International conference on machine learning. PMLR, 2020: 1597-1607.
- He K, Fan H, Wu Y, et al. Momentum contrast for unsupervised visual representation learning[C]//Proceedings of the IEEE/CVF conference on computer vision and pattern recognition. 2020: 9729-9738.
- Grill J B, Strub F, Altché F, et al. Bootstrap your own latent-a new approach to self-supervised learning[J]. Advances in neural information processing systems, 2020, 33: 21271-21284.
- Zhou J, Wei C, Wang H, et al. ibot: Image bert pre-training with online tokenizer[J]. arXiv preprint arXiv:2111.07832, 2021.
- Caron M, Touvron H, Misra I, et al. Emerging properties in self-supervised vision transformers[C]//Proceedings of the IEEE/CVF international conference on computer vision. 2021: 9650-9660.
- Stojnic V, Risojevic V. Self-supervised learning of remote sensing scene representations using contrastive multiview coding[C]//Proceedings of the IEEE/CVF Conference on Computer Vision and Pattern Recognition. 2021: 1182-1191.
- Ayush K, Uzkent B, Meng C, et al. Geography-aware self-supervised learning[C]//Proceedings of the IEEE/CVF International Conference on Computer Vision. 2021: 10181-10190.
- Manas O, Lacoste A, Giró-i-Nieto X, et al. Seasonal contrast: Unsupervised pre-training from uncurated remote sensing data[C]//Proceedings of the IEEE/CVF International Conference on Computer Vision. 2021: 9414-9423.
- Scheibenreif L, Hanna J, Mommert M, et al. Self-supervised vision transformers for land-cover segmentation and classification[C]//Proceedings of the IEEE/CVF Conference on Computer Vision and Pattern Recognition. 2022: 1422-1431.
- Prexl J, Schmitt M. Multi-modal multi-objective contrastive learning for sentinel-1/2 imagery[C]//Proceedings of the IEEE/CVF Conference on Computer Vision and Pattern Recognition. 2023: 2136-2144.
- Jain P, Schoen-Phelan B, Ross R. Self-supervised learning for invariant representations from multi-spectral and SAR images[J]. IEEE Journal of Selected Topics in Applied Earth Observations and Remote Sensing, 2022, 15: 7797-7808.

- Wang Y, Albrecht C M, Braham N A A, et al. DeCUR: decoupling common & unique representations for multimodal self-supervision[J]. arXiv preprint arXiv:2309.05300, 2023.
- Duan P H, Xie Z J, Kang X D, et al. Self-supervised learning-based oil spill detection of hyperspectral images[J]. Science China Technological Sciences, 2022, 65(4): 793-801.
- Wang M, Gao F, Dong J, et al. Nearest neighbor-based contrastive learning for hyperspectral and LiDAR data classification[J]. IEEE Transactions on Geoscience and Remote Sensing, 2023, 61: 1-16.
- Feng Y, Wang P, Diao W, et al. A self-supervised cross-modal remote sensing foundation model with multi-domain representation and cross-domain fusion[C]//IGARSS 2023-2023 IEEE International Geoscience and Remote Sensing Symposium. IEEE, 2023: 2239-2242.
- Alkhalefi M, Leontidis G, Zhong M. LeOCLR: Leveraging Original Images for Contrastive Learning of Visual Representations[J]. arXiv preprint arXiv:2403.06813, 2024.
- Kang J, Fernandez-Beltran R, Duan P, et al. Deep unsupervised embedding for remotely sensed images based on spatially augmented momentum contrast[J]. IEEE Transactions on Geoscience and Remote Sensing, 2020, 59(3): 2598-2610.
- Jung H, Oh Y, Jeong S, et al. Contrastive self-supervised learning with smoothed representation for remote sensing[J]. IEEE Geoscience and Remote Sensing Letters, 2021, 19: 1-5.
- Peng X, Wang K, Zhu Z, et al. Crafting better contrastive views for siamese representation learning[C]//Proceedings of the IEEE/CVF conference on computer vision and pattern recognition. 2022: 16031-16040.
- Mishra S, Shah A, Bansal A, et al. Object-aware cropping for self-supervised learning[J]. arXiv preprint arXiv:2112.00319, 2021.
- Muhtar D, Zhang X, Xiao P. Index your position: A novel self-supervised learning method for remote sensing images semantic segmentation[J]. IEEE Transactions on Geoscience and Remote Sensing, 2022, 60: 1-11.
- Xie Z, Lin Y, Zhang Z, et al. Propagate yourself: Exploring pixel-level consistency for unsupervised visual representation learning[C]//Proceedings of the IEEE/CVF conference on computer vision and pattern recognition. 2021: 16684-16693.
- Liu S, Li Z, Sun J. Self-emd: Self-supervised object detection without imagenet[J]. arXiv preprint arXiv:2011.13677, 2020.
- Song K, Zhang S, Luo Z, et al. Semantics-consistent feature search for self-supervised visual representation learning[C]//Proceedings of the IEEE/CVF International Conference on Computer Vision. 2023: 16099-16108.
- Karra K, Kontgis C, Statman-Weil Z, et al. Global land use/land cover with Sentinel 2 and deep learning[C]//2021 IEEE international geoscience and remote sensing symposium IGARSS. IEEE, 2021: 4704-4707.
- Tao C, Qi J, Zhang G, et al. TOV: The original vision model for optical remote sensing image understanding via self-supervised learning[J]. IEEE Journal of Selected Topics in Applied Earth Observations and Remote Sensing, 2023, 16: 4916-4930.
- Xia G S, Hu J, Hu F, et al. AID: A benchmark data set for performance evaluation of aerial scene classification[J]. IEEE Transactions on Geoscience and Remote Sensing, 2017, 55(7): 3965-3981.
- Long Y, Xia G S, Li S, et al. On creating benchmark dataset for aerial image interpretation: Reviews, guidances, and million-aid[J]. IEEE Journal of selected topics in applied earth observations and remote sensing, 2021, 14: 4205-4230.
- Oquab M, Darcet T, Moutakanni T, et al. Dinov2: Learning robust visual features without supervision[J]. arXiv preprint arXiv:2304.07193, 2023.
- Dosovitskiy A. An image is worth 16x16 words: Transformers for image recognition at scale[J]. arXiv preprint arXiv:2010.11929, 2020.
- Chen Z, Duan Y, Wang W, et al. Vision transformer adapter for dense predictions[J]. arXiv preprint arXiv:2205.08534, 2022.
- Loshchilov I, Hutter F. Decoupled weight decay regularization[J]. arXiv preprint arXiv:1711.05101, 2017.
- Wang D, Zhang Q, Xu Y, et al. Advancing plain vision transformer toward remote sensing foundation model[J]. IEEE Transactions on Geoscience and Remote Sensing, 2022, 61: 1-15.
- Cong Y, Khanna S, Meng C, et al. Satmae: Pre-training transformers for temporal and multi-spectral satellite imagery[J]. Advances in Neural Information Processing Systems, 2022, 35: 197-211.
- Ayush K, Uzkent B, Meng C, et al. Geography-aware self-supervised learning[C]//Proceedings of the IEEE/CVF International Conference on Computer Vision. 2021: 10181-10190.
- Wang Y, Braham N A A, Xiong Z, et al. SSL4EO-S12: A large-scale multimodal, multitemporal dataset for self-supervised learning in Earth observation [Software and Data Sets][J]. IEEE Geoscience and Remote Sensing Magazine, 2023, 11(3): 98-106.

- Mall U, Hariharan B, Bala K. Change-aware sampling and contrastive learning for satellite images[C]//Proceedings of the IEEE/CVF Conference on Computer Vision and Pattern Recognition. 2023: 5261-5270.
- Bastani F, Wolters P, Gupta R, et al. Satlaspretrain: A large-scale dataset for remote sensing image understanding[C]//Proceedings of the IEEE/CVF International Conference on Computer Vision. 2023: 16772-16782.
- Mendieta M, Han B, Shi X, et al. Towards geospatial foundation models via continual pretraining[C]//Proceedings of the IEEE/CVF International Conference on Computer Vision. 2023: 16806-16816.
- Guo X, Lao J, Dang B, et al. Skysense: A multi-modal remote sensing foundation model towards universal interpretation for earth observation imagery[C]//Proceedings of the IEEE/CVF Conference on Computer Vision and Pattern Recognition. 2024: 27672-27683.
- Sun X, Wang P, Lu W, et al. RingMo: A remote sensing foundation model with masked image modeling[J]. IEEE Transactions on Geoscience and Remote Sensing, 2022, 61: 1-22.
- Sherrah J. Fully convolutional networks for dense semantic labelling of high-resolution aerial imagery[J]. arXiv preprint arXiv:1606.02585, 2016.
- Chen H, Shi Z. A spatial-temporal attention-based method and a new dataset for remote sensing image change detection[J]. Remote Sensing, 2020, 12(10): 1662.
- Xiao T, Liu Y, Zhou B, et al. Unified perceptual parsing for scene understanding[C]//Proceedings of the European conference on computer vision (ECCV). 2018: 418-434.
- Qi X, Zhu P, Wang Y, et al. MLRSNet: A multi-label high spatial resolution remote sensing dataset for semantic scene understanding[J]. ISPRS Journal of Photogrammetry and Remote Sensing, 2020, 169: 337-350.
- Li W, Chen K, Chen H, et al. Geographical knowledge-driven representation learning for remote sensing images[J]. IEEE Transactions on Geoscience and Remote Sensing, 2021, 60: 1-16.
- Xiao Z, Long Y, Li D, et al. High-resolution remote sensing image retrieval based on CNNs from a dimensional perspective[J]. Remote Sensing, 2017, 9(7): 725.
- Christie G, Fendley N, Wilson J, et al. Functional map of the world[C]//Proceedings of the IEEE Conference on Computer Vision and Pattern Recognition. 2018: 6172-6180.
- Yang Y, Newsam S. Bag-of-visual-words and spatial extensions for land-use classification[C]//Proceedings of the 18th SIGSPATIAL international conference on advances in geographic information systems. 2010: 270-279.
- Wang J, Zheng Z, Ma A, et al. LoveDA: A remote sensing land-cover dataset for domain adaptive semantic segmentation. arXiv 2021[J]. arXiv preprint arXiv:2110.08733.
- Li K, Wan G, Cheng G, et al. Object detection in optical remote sensing images: A survey and a new benchmark[J]. ISPRS journal of photogrammetry and remote sensing, 2020, 159: 296-307.
- Chen H, Qi Z, Shi Z. Remote sensing image change detection with transformers[J]. IEEE Transactions on Geoscience and Remote Sensing, 2021, 60: 1-14.
- Ren S, He K, Girshick R, et al. Faster r-cnn: Towards real-time object detection with region proposal networks[J]. Advances in neural information processing systems, 2015, 28.
- Li W, Chen K, Shi Z. Geographical supervision correction for remote sensing representation learning[J]. IEEE Transactions on Geoscience and Remote Sensing, 2022, 60: 1-20.
- Cha K, Seo J, Lee T. A billion-scale foundation model for remote sensing images[J]. arXiv preprint arXiv:2304.05215, 2023.
- Huang Z, Zhang M, Gong Y, et al. Generic knowledge boosted pretraining for remote sensing images[J]. IEEE Transactions on Geoscience and Remote Sensing, 2024, 62: 1-13.
- Chu G, Potetz B, Wang W, et al. Geo-aware networks for fine-grained recognition[C]//Proceedings of the IEEE/CVF International Conference on Computer Vision Workshops. 2019: 0-0.
- Wang D, Zhang J, Xu M, et al. Mtp: Advancing remote sensing foundation model via multi-task pretraining[J]. IEEE Journal of Selected Topics in Applied Earth Observations and Remote Sensing, 2024.
- Wang F, Wang H, Wang D, et al. Scaling efficient masked autoencoder learning on large remote sensing dataset[J]. arXiv e-prints, 2024: arXiv: 2406.11933.